Normal and shear strain imaging using 2D deformation tracking on beam steered linear array datasets

Haiyan Xu[a] and Tomy Varghese[b]
Department of Medical Physics, University of Wisconsin–Madison, Madison, Wisconsin 53705 and Department of Electrical and Computer Engineering, University of Wisconsin–Madison, Madison, Wisconsin 53705

(Received 6 July 2012; revised 14 November 2012; accepted for publication 15 November 2012; published 20 December 2012)

Purpose: Previous publications have reported on the use of one-dimensional cross-correlation analysis with beam-steered echo signals. However, this approach fails to accurately track displacements at larger depths (>4.5 cm) due to lower signal-to-noise. In this paper, the authors present the use of adaptive parallelogram shaped two-dimensional processing blocks for deformation tracking.
Methods: Beam-steered datasets were acquired using a VFX 9L4 linear array transducer operated at a 6 MHz center frequency for steered angles from −15 to 15° in increments of 1°, on both uniformly elastic and single-inclusion tissue-mimicking phantoms. Echo signals were acquired to a depth of 65 mm with the focus set at 40 mm corresponding to the center of phantom. Estimated angular displacements along and perpendicular to the beam direction are used to compute axial and lateral displacement vectors using a least-squares approach. Normal and shear strain tensor component are then estimated based on these displacement vectors.
Results: Their results demonstrate that parallelogram shaped two-dimensional deformation tracking significantly improves spatial resolution (factor of 7.79 along the beam direction), signal-to-noise (5 dB improvement), and contrast-to-noise (8–14 dB improvement) associated with strain imaging using beam steering on linear array transducers.
Conclusions: Parallelogram shaped two-dimensional deformation tracking is demonstrated in beam-steered radiofrequency data, enabling its use in the estimation of normal and shear strain components.
 [http://dx.doi.org/10.1118/1.4770272]

Key words: breast cancer, beam steering, angular compounding, normal and shear strain

I. INTRODUCTION

Feasibility of utilizing shear strain imaging to classify and differentiate benign from malignant breast masses based on their bonding information (lesion mobility) has been shown in previous *in vivo* studies.[1–4] However, due to the significantly lower lateral resolution associated with current clinical ultrasound systems, when compared to the axial resolution, most of the studies utilize only the axial-shear strain component instead of the full-shear strain component.[2,3] Our previous comparison study between the axial-shear and full-shear strain tensor demonstrate that full-shear strain imaging provides improved accuracy and robust results for breast tumor classification, especially for asymmetrical positioning of the mass with respect to the applied deformation.[1] Accurate estimation of the lateral displacement vector and strain tensor can help improve the feasibility of utilizing full-shear strain imaging and thereby improve breast tumor classification.

Spatial resolution describes a system's ability to distinguish between two closely situated objects, and includes both the axial resolution (along beam direction) and lateral resolution (perpendicular to beam direction). Previous studies have demonstrated tradeoffs between the elastographic signal-to-noise ratio (SNR_e), contrast-to-noise ratio (CNR_e), and axial resolution.[5–7] In general, larger cross-correlation window lengths for 1D processing[5–7] and kernel dimensions for two-dimensional (2D) processing may improve SNR_e and CNR_e at the cost of the axial resolution.[7] The effort on improving spatial resolution has focused on reduction in the window lengths for 1D processing[5–8] and kernel dimensions for 2D processing.[2,9] On the other hand, lateral resolution for 1D processing is primarily affected by the beam width and line density.[10] However, there was no statistically significant relationship associated with lateral resolution and 1D window length.[10] Further study is required to determine the impact of the lateral extent of the 2D kernel on lateral spatial resolution with 2D processing.

Different approaches have been developed to improve lateral displacement estimation as described in previously published studies.[11–25] Methods proposed include use of the tissue incompressibility assumption,[16] interpolation between radiofrequency (RF) lines[19,20] to improve the line density, interpolation for cross-correlation displacement tracking[17,18,25] to provide subsample estimation of the displacement, multidimensional processing,[23,24] and angular insonifications.[11–15,21,26–30]

Our group has developed novel approaches that utilize angular displacements estimated from beam-steered RF echo data pairs to improve accuracy of the estimated lateral displacement vector.[13,15,26] Based on the assumption that noise artifacts are independent and identically distributed, Techavipoo *et al.*[27,28] developed a least-squares approach to estimate both normal and shear strain tensors using RF data acquired with phased array transducers. Rao *et al.*[12,29] modified this approach for linear array transducers using 1D cross-correlation based analysis. In addition, Rao *et al.*[14] also

implemented an approach using lateral shear deformations. Quantitative experimental results with spatial angular compounding demonstrate that least-squares compounding provides significant improvement in the SNR_e and CNR_e, when compared to weighted-compounding.[11] Chen and Varghese[26] extended the least-squares approach by incorporating a cross-correlation matrix of displacement noise errors into the strain estimation process thereby avoiding any other assumptions for simplifying estimation noise. In addition, angular compounding has been used to estimate variations in attenuation to reduce shadowing of spatially compounded images[31] and for Young's modulus[32] reconstructions.

We have previously demonstrated the presence of decorrelation noise artifacts associated with 1D cross correlation based deformation tracking especially at increased depths in a phantom.[1] This is due to the reduced sonographic SNR associated with echo signals at deeper locations due to tissue attenuation.[33] A more robust deformation tracking approach is therefore necessary. Hansen *et al.*[21] presented a approach utilizing 2D block matching based deformation tracking to estimate axial displacements. However, this approach utilizes lateral displacement information from only two beam-steered angles and utilize a geometrical rotational transformation to register these displacements onto the 0° Cartesian spatial grid.[15,27] Azar *et al.*[30] have also demonstrated the improved performance of 2D tracking using beam steering for estimating the lateral component of the displacement vector.

In this paper, we present the use of parallelogram shaped 2D processing blocks for deformation tracking that vary with the beam-steering angle to estimate the 2D angular displacement vector under a quasistatic deformation.[34] Orthogonal axial and lateral components are then estimated from the 2D angular displacements after a geometrical shear transformation to first register these displacements onto the 0° Cartesian spatial grid and utilizing a least-squares approach. A gradient of the axial displacement vector is utilized to estimate axial strain and axial-shear strain tensors. In a similar manner, the lateral displacement vector is used to estimate the lateral strain and lateral-shear strain tensors. Full-shear strain images were then calculated from the axial-shear and lateral-shear strain tensors. The performance of our 2D deformation tracking method is compared to previously utilized 1D deformation tracking method using tissue-mimicking (TM) phantom experiments. Quantitative experimental results obtained from uniformly elastic TM phantom using 2D deformation tracking demonstrate the significant improvement in SNR_e obtained, compared to 1D tracking. Single ellipsoidal inclusion TM phantoms also demonstrate the improvements in CNR_e obtained when compared to 1D processing.

II. MATERIALS AND METHODS

II.A. TM phantoms

A uniformly elastic TM phantom with dimensions ($100 \times 100 \times 100$) mm^3 was used to compare SNR_e improvements between 1D and 2D deformation tracking methods for beam-steered data. In addition, four single-inclusion TM phantoms were used to evaluate CNR_e improvements for the two deformation tracking approaches. An ellipsoidal mass with dimensions ($19 \times 14 \times 14$) mm^3 was embedded within the center of a uniformly elastic cubical background with dimensions ($80 \times 80 \times 80$) mm^3. We have previously reported on axial- and full-shear strain images obtained with these phantoms in Ref. 1, where 1D processing was utilized to generate the full-shear images from beam-steered data.

All the TM phantoms were manufactured in our laboratory, and acoustic and elastic properties of phantom materials have been previously described.[35,36] The Young's modulus values for both background and inclusion materials in the ellipsoidal phantoms were obtained using dynamic mechanical testing using an EnduraTEC ELF 3220 (Bose Corporation,

TABLE I. Mean and standard deviation of the strain stiffness contrast for the ellipsoidal inclusion TM phantoms for different angular increments for the 1D and 2D deformation tracking approaches.

Phantom	Modulus contrast	Method		Angular increments 1°	3°	5°	15°
Unbound ellipsoid (0°/90°)	4.2	1D	Mean SSC	2.11	2.12	2.17	1.95
			Std	0.29	0.30	0.27	0.22
		2D	Mean SSC	2.11	2.08	2.09	2.08
			Std	0.04	0.03	0.03	0.06
Unbound ellipsoid (30°/60°)	3.2	1D	Mean SSC	2.09	2.05	2.13	2.08
			Std	0.23	0.14	0.23	0.11
		2D	Mean SSC	2.11	2.07	2.07	2.00
			Std	0.09	0.11	0.11	0.12
Bound ellipsoid (0°/90°)	4.2	1D	Mean SSC	2.07	2.14	2.06	1.88
			Std	0.18	0.18	0.20	0.30
		2D	Mean SSC	2.10	2.12	2.10	2.11
			Std	0.10	0.07	0.06	0.06
Bound ellipsoid (30°/60°)	3.2	1D	Mean SSC	2.2	2.19	2.06	1.60
			Std	0.58	0.61	0.40	0.44
		2D	Mean SSC	1.96	1.96	1.96	1.93
			Std	0.03	0.05	0.04	0.07

TABLE II. Mean and standard deviation of the strain stiffness contrast for the ellipsoidal inclusion TM phantoms for different maximum beam steered angles for the 1D and 2D deformation tracking approaches.

Phantom	Modulus contrast	Method		Maximum steered angle (°)				
				3°	6°	9°	12°	15°
Unbound ellipsoid (0°/90°)	4.2	1D	Mean SSC	2.15	2.16	2.20	2.17	2.11
			Std	0.12	0.16	0.29	0.30	0.29
		2D	Mean SSC	2.12	2.13	2.12	2.11	2.11
			Std	0.05	0.04	0.05	0.05	0.04
Unbound ellipsoid (30°/60°)	3.2	1D	Mean SSC	2.14	2.17	2.17	2.13	2.09
			Std	0.14	0.19	0.21	0.20	0.23
		2D	Mean SSC	2.06	2.05	2.05	2.06	2.11
			Std	0.11	0.10	0.10	0.10	0.09
Bound ellipsoid (0°/90°)	4.2	1D	Mean SSC	2.01	2.10	2.13	2.27	2.07
			Std	0.25	0.25	0.21	0.60	0.18
		2D	Mean SSC	2.15	2.15	2.13	2.1	2.10
			Std	0.07	0.07	0.07	0.09	0.10
Bound ellipsoid (30°/60°)	3.2	1D	Mean SSC	2.01	2.10	2.13	2.27	2.07
			Std	0.25	0.25	0.21	0.60	0.18
		2D	Mean SSC	2.15	2.15	2.13	2.11	2.10
			Std	0.07	0.07	0.07	0.09	0.10

EnduraTEC Systems Group, Minnetonka, MN) and has been reported in Ref. 1. The contrast of each phantom was estimated from the ratio of Young's modulus between the inclusion and background material as also shown in Tables I and II, respectively.

The ellipsoidal inclusion phantoms contained either a bound inclusion (i.e., mass firmly attached to background material mimicking malignant breast masses) or an unbound inclusion (i.e., mass loosely attached to the background mimicking benign masses). The inclusion phantom pair either had a symmetrical ellipsoidal inclusion oriented at 0°/90°, or asymmetrical inclusions oriented at 30°/60° to the top surface of the phantom. Both the uniform and ellipsoidal inclusion phantoms were scanned using a Siemens S2000 real-time clinical scanner (Siemens ultrasound, Mountain View, CA) equipped with a VFX 9L4 linear array transducer. The transducer was operated at a 6 MHz center frequency, 80% bandwidth, and a sampling frequency of 40 MHz. Echo signals were collected up to a depth of 65 mm with a single focus set at a depth of 40 mm, which also corresponds to the center of the four ellipsoidal inclusion phantoms. Beam-steered RF data were acquired from −15° to 15° in increments of 1°. Thus, 31 pairs of RF beam-steered data frames were acquired before and after an applied deformation. Note that only a single deformation of 1% (1 or 0.8 mm) of the phantom height was applied to the phantom using a positioning stage. The transducer was embedded in a compressional plate larger than the TM phantom surface to provide a uniform deformation over the entire TM phantom surface.

II.B. Angular and displacement vector estimation

Angular displacement vectors (along and perpendicular to the beam direction) at each beam steered angle (θ°) were estimated from the pre- and postdeformation echo signals using parallelogram shaped 2D cross correlation based displacement estimation. The parallelogram shaped kernel dimensions was 0.385 mm along the beam direction ×3 RF-lines, with a 75% overlap along beam direction and a lateral step of one RF-line along its perpendicular direction. Note that the angular displacement pairs were estimated from a Cartesian spatial grid obtained for each beam steered angle.

In order to register angular displacements obtained for each beam-steered angle, the estimated angular displacement vectors were first smoothed using spline interpolation along each beam-steered angle. The angular displacement vectors from each angular Cartesian spatial grid were then transferred and registered into the Cartesian spatial grid obtained for the 0° RF data. A geometrical shear transformation shown in Eq. (1) was utilized to perform the transformation to the 0° Cartesian grid, shown as follows:

$$z = zt_\theta,$$
$$x = \tan(\theta) \times zt_\theta + xt_\theta, \quad (1)$$

where θ represents each beam-steering angle ranging from −15° to 15°, zt_θ and xt_θ represent the axial and lateral coordinates of each beam steered Cartesian spatial grid, respectively, and z and x denote the axial and lateral coordinates of the 0° Cartesian spatial grid.

Comparisons between the Cartesian spatial grid obtained for 8° beam-steered data and its corresponding shear transformation within the Cartesian spatial grid obtained along the 0° direction is shown in Figs. 1(a)–1(d), where (a) represents the spatial grid for the 8° beam-steered angle and (b) represents its corresponding shear geometrical transformation within the spatial grid for the 0° coordinate system. Note that a rectangular spatial grid within the steered coordinates was transformed into a parallelogram shape within the 0° coordinates. Based on this spatial grid and shear transformation, both the angular displacement vectors were transferred onto the spatial grid

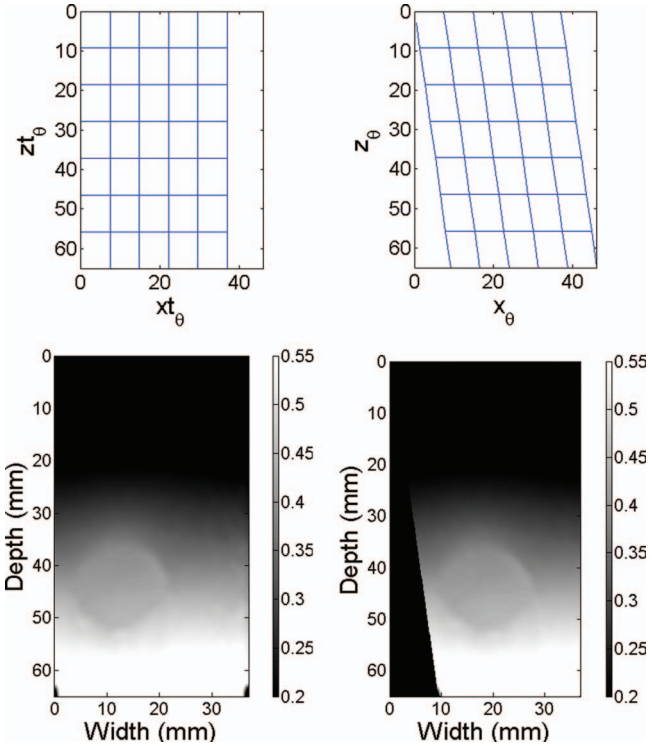

FIG. 1. Shear transformation for the spatial grid (top), along with the angular displacement vector. The left column shows the spatial grid and angular displacements obtained using a 8° beam-steered angle, respectively. The right column shows the spatial grid and angular displacement on a 0° spatial grid.

obtained for the 0° RF data using two-dimensional interpolation. Figures 1(c) and 1(d) show the angular displacement vector along the beam-steered angle (8°) for the symmetrical bound ellipsoidal phantom, while Fig. 1(c) presents the experimental phantom results obtained within its beam-steered coordinates and Fig. 1(d) presents its corresponding shear transformation results for the 0° coordinates. In a similar manner, all the angular displacement vectors were shear transformed to the same Cartesian spatial grid using interpolation for each beam-steered angle.

For each point O in space from a single beam-steered acquisition, its total displacement vector $\vec{d}$ is observed and tracked using 2D deformation tracking; both along and perpendicular to the beam-steered direction as shown in Fig. 2. Under the assumption of $\overline{u}_\theta$ as a unit vector along the beam-steered angle θ and $\overline{u}_\theta^T$ as a unit vector perpendicular to the beam-steered direction. Let pz_θ denote the projection of the total displacement vector $\vec{d}$ in the beam-steered direction and px_θ be its projection onto the unit vector $\overline{u}_\theta^T$ perpendicular to the beam-steered direction. Thus, the projection can be expressed as the dot product between the total displacement and the projected directional unit vector as shown in Eq. (2)

$$\begin{bmatrix} pz_\theta \\ px_\theta \end{bmatrix} = \begin{bmatrix} \vec{d}\cdot\overline{u}_\theta \\ \vec{d}\cdot\overline{u}_\theta^T \end{bmatrix} = \begin{bmatrix} \cos\theta & \sin\theta \\ -\sin\theta & \cos\theta \end{bmatrix} \begin{bmatrix} d_z \\ d_x \end{bmatrix}, \tag{2}$$

where d_z and d_x represent the component of the displacement vector $\vec{d}$ along the z and x direction, respectively, and θ represents the beam-steered angle.

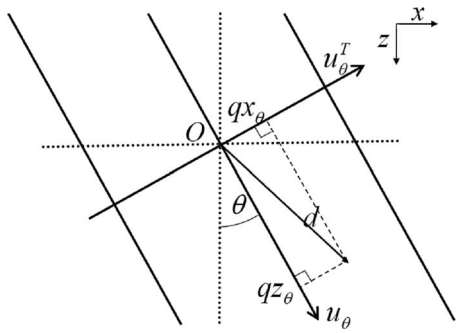

FIG. 2. Projection of the actual displacement vector $\vec{d}$ at point O, onto unit vectors along $\overline{u}_\theta$ and perpendicular to $\overline{u}_\theta^T$ beam steered direction.

All the angular displacement vectors passing through the point O were registered onto the zero-angle grid, and were then used to compute the axial and lateral displacement vector using a 2D least-squares displacement estimator shown in Eq. (3). Previously only the component of the axial and lateral displacement along the beam direction were estimated from the angular displacement vectors using a 1D rotational transformation.[15,21] The contribution of the lateral angular displacement vector to the actual lateral displacement component was calculated based on each spatial angular displacement, using

$$\bar{q} = A\bar{d} + \bar{n}, \tag{3}$$

where

$$\bar{q} = \begin{bmatrix} qz_{\theta_1} \\ qz_{\theta_2} \\ \vdots \\ qz_{\theta_m} \\ qx_{\theta_1} \\ qx_{\theta_2} \\ \vdots \\ qx_{\theta_m} \end{bmatrix}, A = \begin{bmatrix} \cos\theta_1 & \sin\theta_1 \\ \cos\theta_2 & \sin\theta_2 \\ \vdots & \vdots \\ \cos\theta_m & \sin\theta_m \\ -\sin\theta_1 & \cos\theta_1 \\ -\sin\theta_2 & \cos\theta_2 \\ \vdots & \vdots \\ -\sin\theta_m & \cos\theta_m \end{bmatrix}, \bar{d} = \begin{bmatrix} d_z \\ d_x \end{bmatrix},$$

$$\text{and } \bar{n} = \begin{bmatrix} nz_{\theta_1} \\ nz_{\theta_2} \\ \vdots \\ nz_{\theta_m} \\ nx_{\theta_1} \\ nx_{\theta_2} \\ \vdots \\ nx_{\theta_m} \end{bmatrix}.$$

Note that qz_{θ_i} and qx_{θ_i} represent an observation of the displacement vector $\bar{d}$ along and perpendicular to the beam-steered angle θ_i for $i = 1, \ldots, m$, respectively, where m denotes the total number of beam-steered frames acquired. In Eq. (1), A represents the transformation matrix that includes contributions due to the steering angle θ_i along the clockwise direction. Note that d_z and d_x represent the axial and lateral

displacement vector components (relative to the applied deformation), and nz_{θ_i} and nx_{θ_i} denote the noise contributions in the estimated displacements along and perpendicular to each beam-steered angle θ_i, respectively.

The least-squares solution for the displacement vector was previously described by Techavipoo and Varghese[28] and is given by

$$\tilde{d} = (A^{\mathrm{T}}A)^{-1}A^{\mathrm{T}}\bar{q}. \tag{4}$$

We also utilize 2D spline fitting to obtain subsample displacement estimates for both the axial and lateral displacement vectors. The normal and shear strain tensors were then calculated from the axial and lateral displacement vectors using a least-squares strain estimator.

II.C. Estimation of SNR_e, CNR_e, and strain stiffness contrast (SSC)

A selected region of interest (ROI) around the focal depth (40 mm) of the axial and lateral strain tensor images were used to compute SNR_e, CNR_e, and SSC values using both 1D and 2D deformation tracking methods. The SSC is defined as the ratio of the mean strain within the inclusion to that of the background estimated from the axial strain image.[37] Since the strain tensor image was calculated using angular displacements obtained using independent beam-steered data, the number of angular pixels that contribute to the axial and lateral strain tensor image is the largest in the central triangular region and decreases on either side. The isosceles trapezoidal shaped ROI in the strain tensor image that utilizes all available beam-steered contributions during the image registration process was selected for SNR_e analysis. This ROI has a height of 20 mm, a top long edge of 15 mm, and a bottom short edge of 6 mm as shown in Fig. 3(a). The CNR_e analysis, however, was performed using three rectangular shaped ROI, one within the inclusion and two ROIs located in the background at a similar depth as shown in Fig. 3(b). The area of ROI within the inclusion was equal to the sum of two background ROIs, which were placed symmetrically in the background and parallel to the ROI within the inclusion.

The SNR_e in the strain tensor images for uniformly elastic phantoms using both 1D and 2D deformation tracking methods were computed to quantify the respective improvement in the image. The SNR_e is defined as[5,38,39]

$$\mathrm{SNR}_e = \frac{m}{\sigma}, \tag{5}$$

where m and σ represent the mean and standard deviation of the strain estimates in the selected ROI, respectively. We also analyze variations in the SNR_e values for different maximum beam-steered angles and for different beam-steered angular increments.

Ellipsoidal inclusion phantoms were used to estimate the CNR_e and corresponding SSC values, which are defined as follows:[37]

$$\mathrm{CNR}_e = \frac{2(m_i - m_b)^2}{(\sigma_i^2 + \sigma_b^2)}, \tag{6}$$

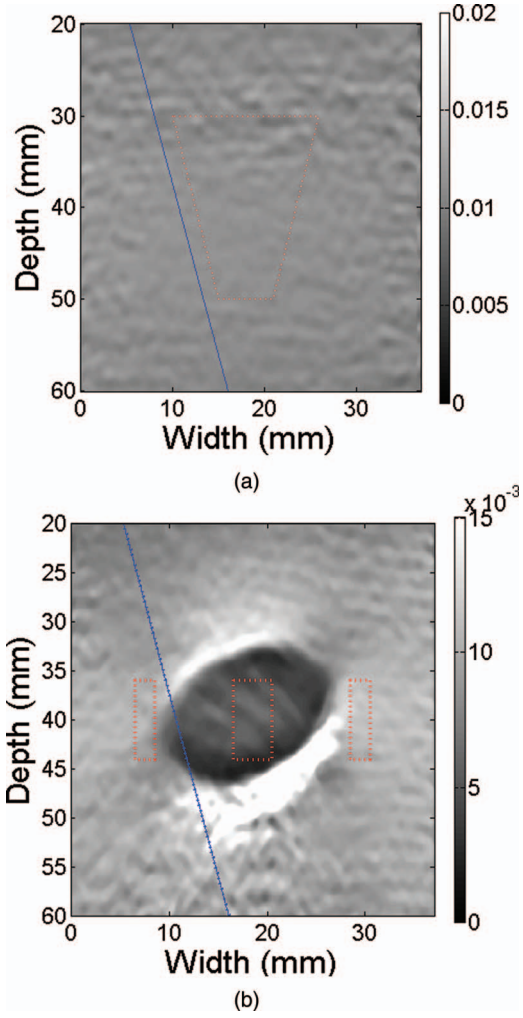

FIG. 3. Axial strain images obtained using 2D beam steered datasets for the uniformly elastic TM phantom (a) and an ellipsoidal inclusion phantom (b). The 0.02 value on the color bar represents a 2% strain. The ROIs shown on the images were used to estimate the SNR_e and CNR_e, respectively. The solid line represents the maximum beam steered angle used for angular compounding.

$$\mathrm{SSC} = \frac{m_i}{m_b}, \tag{7}$$

where m_i and m_b represent the mean strain estimated in the selected ROI within the inclusion and background, respectively, σ_i^2 and σ_b^2 denote the corresponding variance within the inclusion and background ROI, respectively.

In order to obtain statistically significant results, we estimated the mean and standard deviation of SNR_e and CNR_e obtained over ten independent RF data acquisitions. Statistical analysis was based on similarly selected ROI in the strain tensor images. Each independent beam-steered pre- and post-deformation dataset was processed using both 1D and 2D deformation tracking approaches.

III. RESULTS

The plots shown in Figs. 4 and 5 present the mean and standard deviation of the SNR_e estimated over ten independent axial strain tensor images. Figure 4 presents the

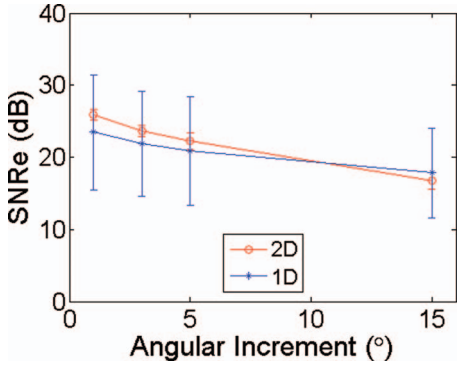

FIG. 4. Plots of the mean SNR_e and standard deviation (error bars) over ten independent RF datasets acquired on a uniformly elastic TM phantom demonstrating the impact of beam steered angular increment for 1D vs 2D deformation tracking.

variation of the SNR_e versus the beam-steered angular increment, for a maximum beam-steered angle of $\pm 15^\circ$, and angular increments of 1°, 3°, 5°, and 15°. Each corresponding strain tensor image was calculated from 31, 11, 5, and 3 beam-steered RF echo signal frame pairs, respectively. Observe that the SNR_e values decrease with a decrease in the total number of angular displacement images used for image registration and compounding for both 1D and 2D deformation tracking for the same maximum beam-steered angle. For the same maximum angle, improved SNR_e is obtained with an increase in the number of angular displacement frames used. Note that 2D deformation tracking provides both higher mean SNR_e values and significantly lower standard deviations indicated by the error bars when more than five beam-steered data frame pairs are used for image registration. The results indicate that 2D tracking is a more robust displacement estimation method. On the other hand, 1D deformation tracking exhibits significantly higher standard deviations which increases the number of angular displacement images needed to obtain a reasonable strain tensor image, when compared to 2D deformation tracking. This is due to increased ultrasound noise artifacts with depth due to attenuation and increased noise artifacts for beam-steered RF data obtained at larger beam insonification angles.

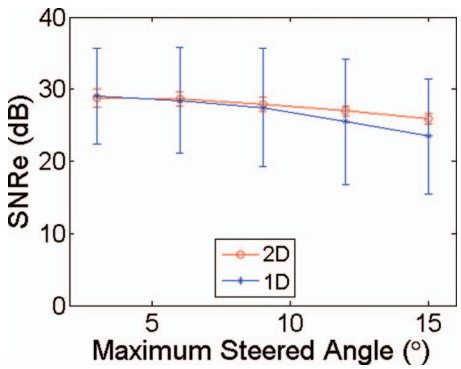

FIG. 5. Plots of mean SNR_e and standard deviation (error bars) over ten independent RF datasets acquired on a uniform TM phantom demonstrating the impact of the maximum beam-steered angle on compounded strain images for 1D vs 2D deformation tracking.

Variation in the SNR_e versus the maximum beam-steered angle used for image registration in increments of 1° is shown in Fig. 5. Observe that the SNR_e slightly decreases with an increase in the maximum angle. This is due to the increased artifacts in beam-steered echo data pairs obtained at larger beam-steered angles. Larger beam-steered angles provide additional lateral displacement information at the cost of higher noise artifacts in the angular displacement images. Note that the 2D deformation tracking method provides stable SNR_e values over all the strain tensor images estimated at different maximum angles. Note that 1D deformation tracking provides a comparable mean SNR_e value to 2D deformation tracking method up to a maximum angle of 6° with the SNR_e dropping with larger maximum angles.

Four ellipsoidal unbound and bound inclusion phantoms described previously were also used to compare deformation tracking performance between the 1D and 2D approaches. Figures 6–8 present the displacement, normal strain, and shear strain images obtained using 1D and 2D approaches for the unbound asymmetrical ellipsoidal inclusion phantom, respectively, with a maximum angle of 15° in increments of 1°. Figure 6 presents compounded axial displacement images (a) and (b), and lateral displacement images (c) and (d) for the asymmetrical (30°) unbound ellipsoidal phantom obtained with both 1D (a) and (c) and 2D (b) and (d) processing. Observe that 2D deformation tracking provides improved accuracy and precision for the axial displacement vector image with obvious and precise mass/background interfaces as shown in Fig. 6(b). While 1D processing also exhibits axial displacement vector images with improved accuracy above the focal depth ($\leq$40 mm) as shown in Fig. 6(a), it fails to track the mass/background interface accurately near the bottom edges of the interface. The mass/background interface is blurred toward the bottom of the inclusion. This is partly due to increased tracking errors with 1D processing, reduced signal-to-noise ratio of the echo signals due to attenuation, and artifacts with beam-steered data at larger insonification angles. As shown in Figs. 6(c) and 6(d), the lateral displacement vector image obtained using 2D deformation tracking provides a smoother image with relatively precise mass/background interfaces when compared to that obtained using 1D deformation tracking.

All of these local displacement vector improvements obtained using 2D processing contribute to the significant enhancement visualized on its corresponding axial and lateral strain tensor image when compared to 1D processing as shown in Fig. 7. The rectangular regions outlined in dotted show the selected ROIs within the inclusion and the background regions. The solid line represents the left edge of maximum beam-steered angle (15°) for the trapezoidal region previously mentioned. Observe that 2D deformation tracking provides precise mass/background interfaces with the inclusion size and shape accurately illustrated in the axial strain tensor image as shown in Fig. 7(b). The fact that 1D processing fails to estimate strain tensor estimates below the focal depth (>40 mm) for the lateral strain tensor as shown in Fig. 7(c) and below the 50 mm for the axial strain tensor as

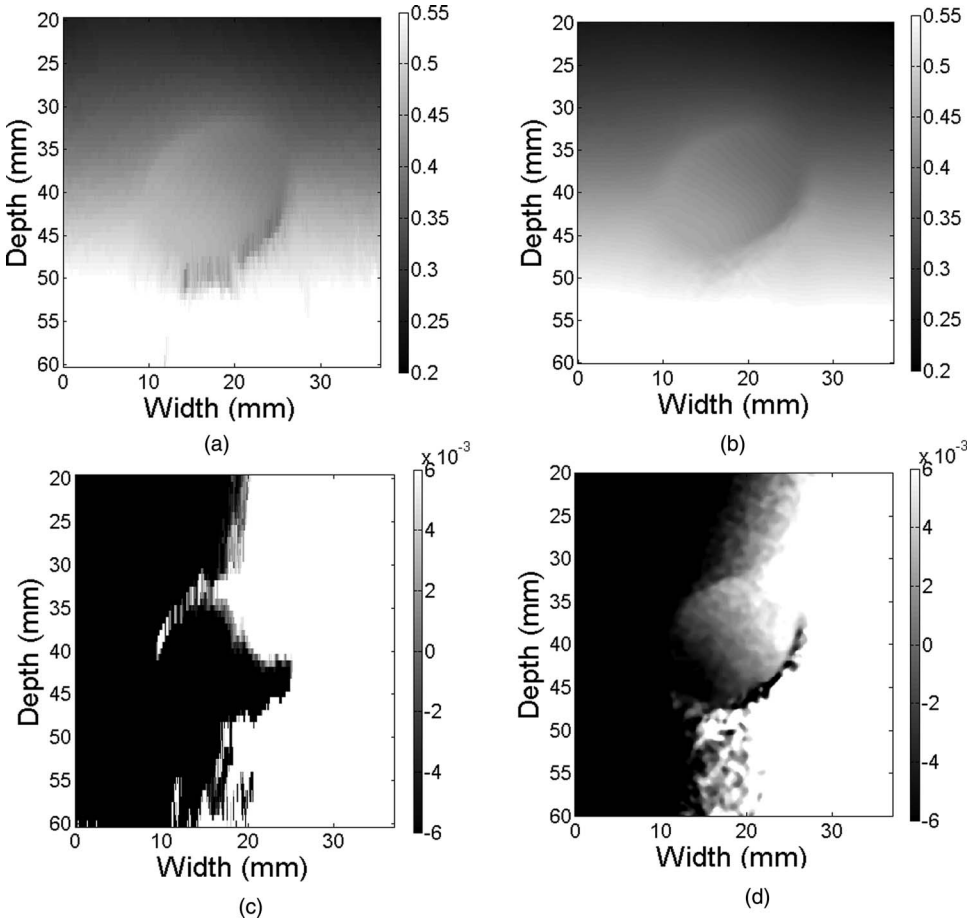

FIG. 6. Axial displacement (a) and (b) and lateral displacement (c) and (d) images obtained using 1D (a) and (c) and 2D (b) and (d), beam steered data for the asymmetric (30°) unbound ellipsoid TM phantom. The units in the color bar for the displacement is in millimeters.

shown in Fig. 7(a). These artifacts are not visible with 2D deformation tracking as illustrated in Figs. 7(b) and 7(d).

Figure 8 presents a comparison of axial-shear strain images (a) and (b) and full-shear strain images (c) and (d) obtained using 1D (a) and (c) and 2D (b) and (d) deformation tracking methods. The blue and red colors in the figure represent different directions for the shear strain. The value of 0.006 on the color bar corresponds to a 0.6% strain. Note that the fact that 1D deformation tracking fails to track deformations deeper than 45 mm is evident in both the axial-shear strain and full-shear strain images. Also observe that 2D deformation tracking provides improved accuracy and precision for the axial-shear and full-shear strain with precise shear strain regions visualized around the mass/background interfaces as shown in Figs. 8(b) and 8(d). Note that the inclusion shape and size are also clearly visualized when compared to the results obtained with 1D deformation tracking. The red and blue shear noise artifacts that appear in the background in the images in Figs. 8(a) and 8(c) is also significantly reduced as observed in Figs. 8(b) and 8(d).

Figure 9 presents the impact of the angular increment on the CNR_e for axial strain tensor images for the four ellipsoidal phantoms for a maximum beam steered angle of $\pm 15°$ and angular increments of 1°, 3°, 5°, and 15°. Here, Fig. 9(a) presents results for the symmetrical unbound ellipsoidal phantom; Fig. 9(b) for the asymmetrical unbound ellipsoidal phantom; Fig. 9(c) for the symmetrical bound ellipsoidal phantom; and Fig. 9(d) for the asymmetrical bound ellipsoidal phantom. The error bars denote the standard deviation of the CNR_e estimated over ten independent experiments. Observe that 2D deformation tracking provides a higher mean CNR_e and significantly lower variance in the image when compared to 1D deformation tracking for the four different ellipsoidal phantoms. The mean CNR_e for unbound masses utilizing 2D deformation tracking method is about 10 dB higher than that obtained using 1D deformation tracking as shown in Figs. 9(a) and 9(b); and about 6 dB for bound masses as presented in Figs. 9(c) and 9(d). Note that for smaller angular increments (1° up to 3°), the CNR_e is almost constant along with the increase in the steered angular increment using 2D processing, however, for larger angular increments, the mean CNR_e decreases along an increase in the angular increment for the four phantoms. On the other hand, the CNR_e is relatively constant with an increase in the angular increment for 1D deformation tracking. This is due to the concomitant increase in artifacts associated with the angular strain image obtained at larger beam steered angles, and the inability of 1D processing to accurately track the deformation in this region.

Mean and standard deviation values of the corresponding SSC estimated versus different beam-steered angular

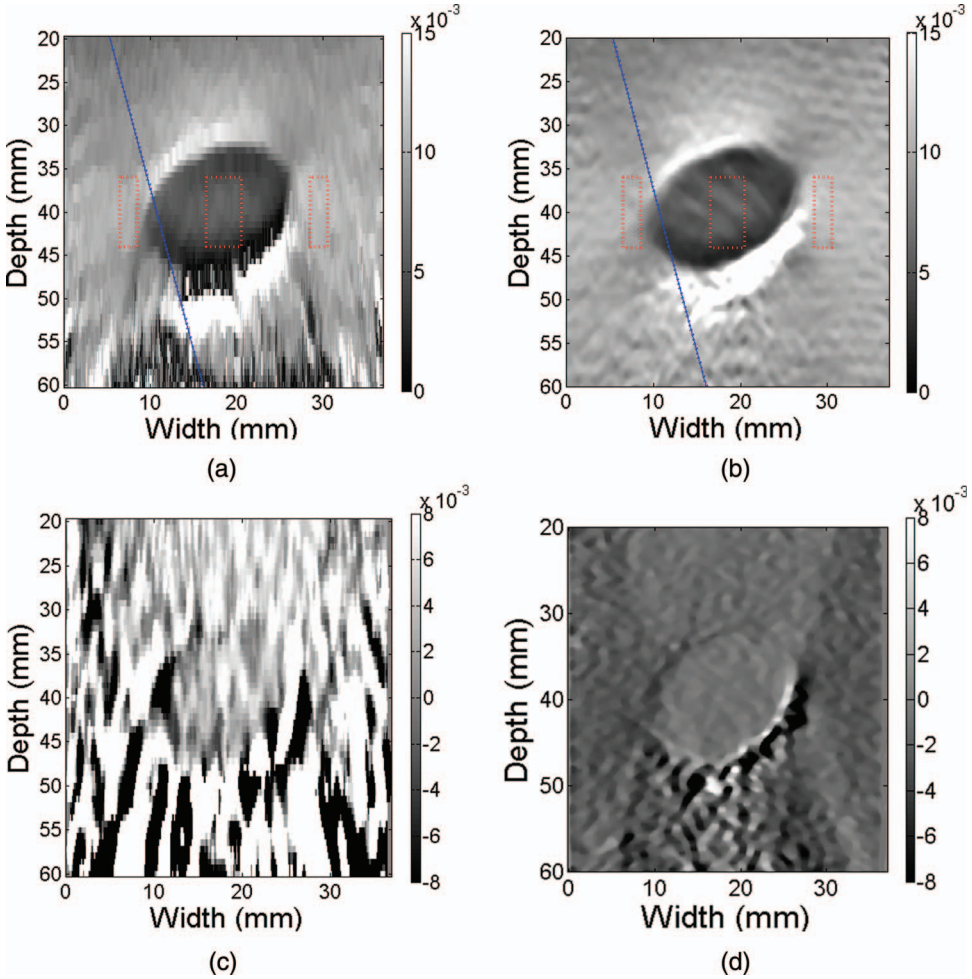

FIG. 7. Axial strain (a) and (b) and lateral strain (c) and (d) images obtained using 1D (a) and (c) and 2D (b) and (d), beam steered data for the asymmetric (30°) bound ellipsoid TM phantom. The 0.008 value on the color bar represents a 0.8% strain. The ROIs shown were used to estimate CNR_e and strain stiffness contrast. The solid line represents the maximum beam steered angle used for angular compounding.

increments used to generate the compounded image is shown in Table I. The mean and standard deviation were estimated over the ten independent experiments corresponding to the CNR_e computations evaluated previously. The actual modulus contrast for the symmetrical bound/unbound ellipsoidal phantom (0°/90°) was 4.2 while that for the asymmetrical bound/unbound ellipsoidal phantoms (30°/60°) was 3.2, respectively. Observe that strain stiffness contrast calculated from axial-strain images over the ROI within the mass and ROI in the background was around 2.1 for the symmetrical phantoms, and 2.0 for the asymmetrical phantoms. For each angular increment, the overall standard deviation obtained using 1D processing was significantly larger than that obtained using 2D processing, ranging from a factor of 1 to about 19 in some instances. For the same phantom, larger beam-steered angles (15°) introduce increased standard deviation with 1D processing when compared to 2D processing. Results are improved with the use of smaller angles (on the order of 1° or 3°). Note that the mean value of the SSC estimated using 2D processing is more consistent than those values obtained using the 1D estimator.

Figure 10 presents a plot of the CNR_e versus the maximum beam-steered angle in increments of 1°. Note that the mean CNR_e plot for the 1D deformation tracking decreases with an increase in the maximum angle. This is due to the increased noise artifacts associated with larger beam-steered angles. Larger beam-steered angles provide additional lateral displacement information, however, with the concomitant increase in noise artifacts due to the larger insonification angles. Note that the standard deviation of the CNR_e plots vary greatly with increased maximum angle especially with 1D tracking. The mean CNR_e calculated using 2D deformation tracking is about 10 dB higher than that estimated using 1D deformation tracking. Observe that the bound ellipsoidal phantom has a larger variation when compared to unbound ellipsoidal phantom. Table II presents the corresponding SSC estimated for different maximum beam-steered angles. The SSC for the compounded strain images obtained using 2D deformation tracking provides consistent results over all the maximum angles used. The symmetrical unbound/bound ellipsoidal phantom pair has a SSC around 2.1. On the other hand, the asymmetrical unbound/bound ellipsoidal phantom pair has a SSC around 2.0, which is similar to the values reported in Table I. For each maximum beam-steered angle, standard deviation values obtained using 1D processing are about 1–7 times larger than the values obtained using 2D

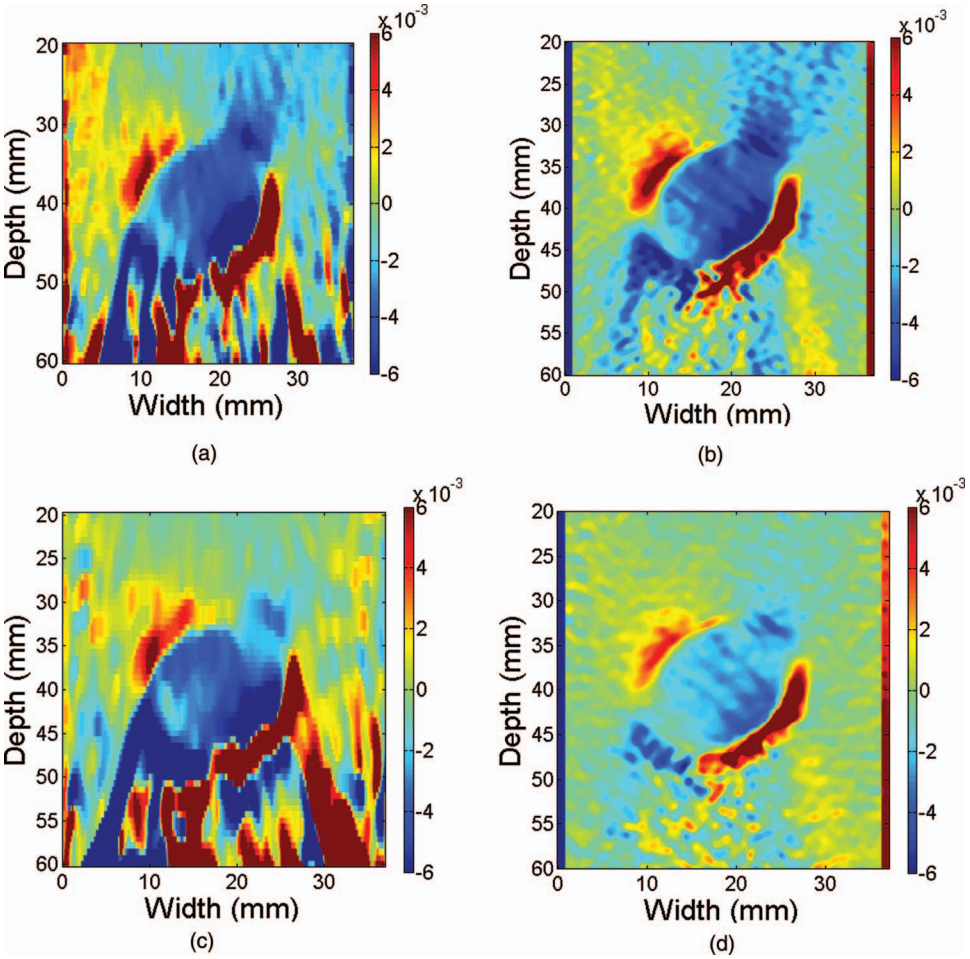

FIG. 8. Axial-shear strain (a) and (b) and full-shear strain (c) and (d) images obtained using 1D (a) and (c) and 2D (b) and (d), beam steered data for the asymmetric (30°) bound ellipsoid TM phantom. The 0.006 value on the color bar represents a 0.6% strain. The ROIs shown were used to estimate CNR_e and strain stiffness contrast.

processing. Bound inclusions exhibit increased variance when compared to unbound inclusions. The mean values across the maximum steered angles are also more consistent with 2D processing.

For both the uniformly elastic and inclusion phantoms, a window length of 3 mm was required to estimate accurate displacements with 1D processing. On the other hand, with 2D processing the 2D parallelogram shaped processing kernels used had dimensions of 0.385 mm ×3 RF-lines to obtain accurate displacement results. Thus, based on the window length,[5–7] the spatial resolution along the beam direction improved by a factor of 7.79 for 2D processing when compared to 1D processing. Both the SNR_e and CNR_e estimates obtained with 1D processing are also lower when compared to that obtained using 2D processing.

IV. DISCUSSION AND CONCLUSIONS

Results obtained with uniformly elastic phantoms in this paper, demonstrate the significant improvement in the spatial resolution and SNR_e obtained with the use of the 2D parallelogram shaped processing kernels (0.385 mm ×3 RF-lines) when compared to that obtained with 1D processing with 3 mm gated rectangular data segments. Spatial resolution improved by a factor around 7 with 2D processing, while the SNR_e with 2D processing is approximately 5 dB better than that obtained with 1D processing. The ROI over which the SNR_e was computed corresponds to the trapezoidal region over which angular displacement estimates from all the beam-steered angles are included in the composite axial-strain image. For the same maximum beam-steered angle, higher SNR_e is obtained with an increase in the number of angular displacements used to obtain the compounded strain images. On the other hand for the same angular increment, an increase in the maximum beam-steered angle slightly reduces the SNR_e obtained using 2D deformation tracking methods. 1D deformation tracking presents similar declines in the SNR_e for maximum angles less than or equal to 6°, however, the performance drops rapidly for maximum angles greater than 6°. In addition, the standard deviation of the compounded axial strain images over ten independent RF datasets utilizing 2D deformation tracking methods is 1/7 of that obtained utilizing 1D deformation tracking, demonstrating that 2D deformation

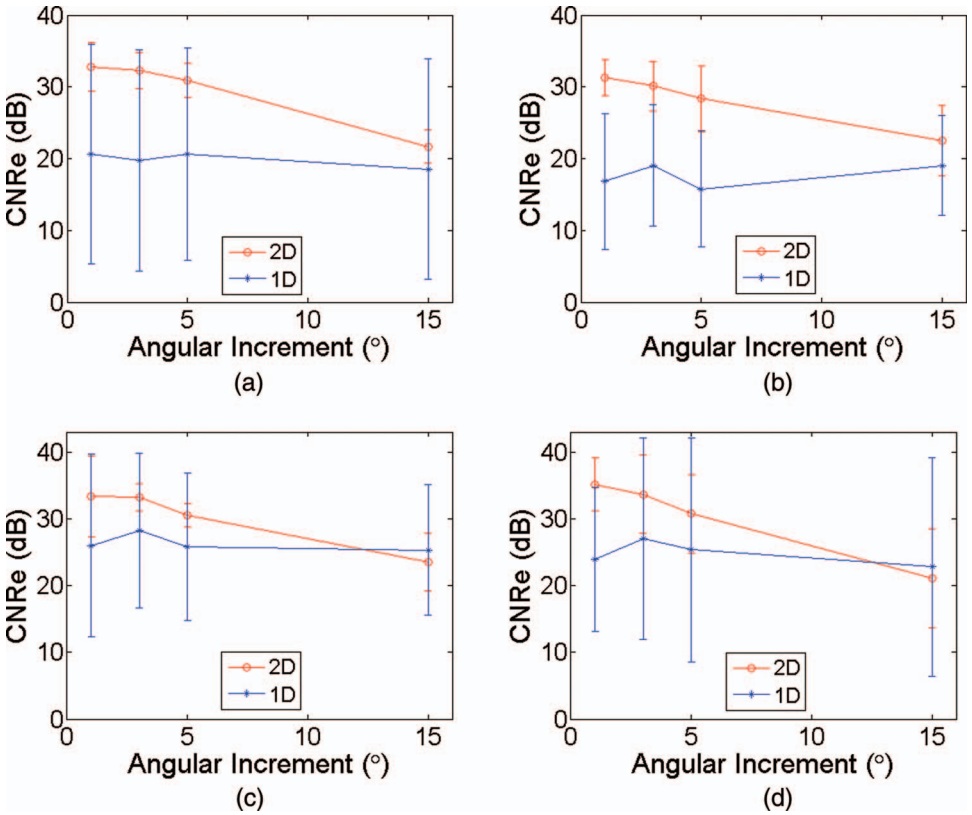

FIG. 9. Plots of mean CNR_e and standard deviation (error bars) over ten independent beam-steered RF datasets acquired on the four ellipsoid TM phantoms demonstrating the impact of the beam steered angular increment for 1D vs 2D processing. The subplots represent results for (a) symmetric unbound, (b) asymmetric unbound, (c) symmetric bound, and (d) asymmetric bound phantoms, respectively.

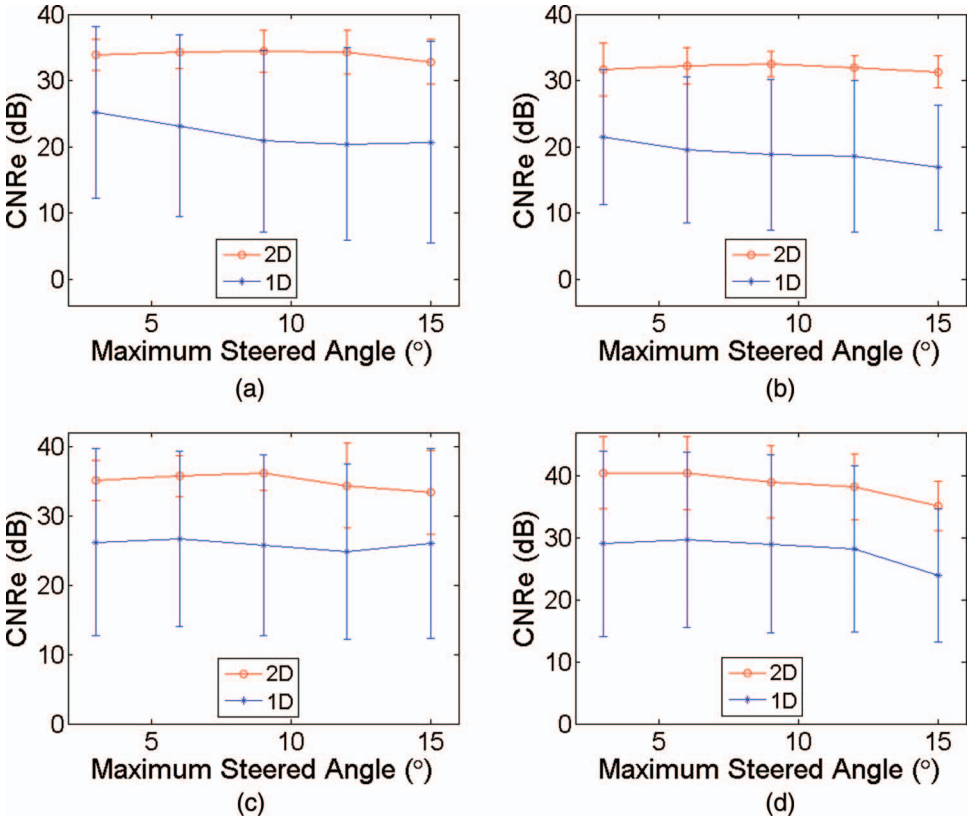

FIG. 10. Plots of mean CNR_e and standard deviation (error bars) over ten independent RF datasets acquired on the four ellipsoid TM phantoms demonstrating the impact of the maximum beam-steered angle for 1D vs 2D processing. The subplots represent results for the (a) symmetric unbound, (b) asymmetric unbound, (c) symmetric bound, and (d) asymmetric bound phantom, respectively.

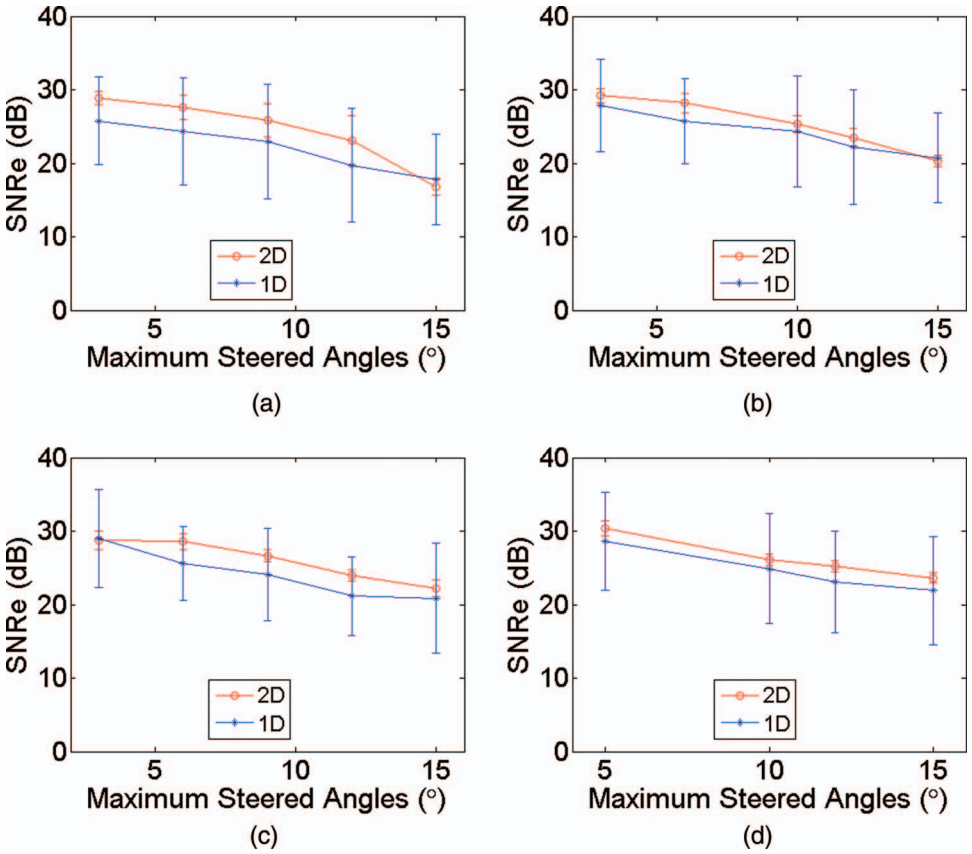

FIG. 11. Plots of mean SNR_e and standard deviation (error bars) over ten independent RF datasets acquired on an uniformly elastic TM phantom demonstrating the impact of different maximum angles on similar number of compounded strain images. Results are shown for 3 beam steered angles (a), 5 beam-steered angles (b), 7 beam-steered angles (c), and 11 beam-steered angles (d), respectively.

tracking is both an accurate and robust deformation tracking method.

Noise artifacts observed below the inclusion with 1D processing were not visible with 2D processing for displacement, strain and shear strain images, demonstrating the superior deformation tracking obtained with 2D tracking, especially for regions with lower signal-to-noise. Lateral strain images that were poorly tracked using the 1D deformation tracking approach are significantly improved with 2D processing. In addition, 2D deformation tracking provides clear and smooth inclusion/background interfaces over the entire image, where these interfaces clearly differentiate the inclusions for both unbound and bound masses. Asymmetrical inclusion phantoms poorly tracked with 1D processing are clearly visualized with 2D processing. Background noise artifacts in strain images observed with 1D processing were significantly reduced using 2D processing.

Experimental results for the ellipsoidal phantoms show that the 2D parallelogram shaped processing blocks for deformation tracking provide a significant improvement in the CNR_e of 14 dB for unbound masses and 8 dB for bound masses, respectively, for a maximum angle of 15°, when compared to results obtained using 1D deformation tracking. The CNR_e curves presented in Fig. 9 exhibit saturation for smaller angular increments, which corresponds to results presented in Ref. 11. For smaller angular increments, the angular displacements obtained are highly correlated, and an angular increment of approximately 3° is enough to obtain accurate compounded strain images using either 1D or 2D deformation tracking methods. Since the error bars for 1D processing are significantly larger than those for 2D processing, there is some overlap between the error bars for the two methods. However, note the length of the error bars for 2D processing when compared to 1D deformation tracking, which partly indicates the robustness of the 2D deformation tracking approach described in this paper.

The focus in this paper was on the evaluation of improvements in the axial strain with angular compounding. Our results in Fig. 3 demonstrate that although the SNR_e decreases with a reduction in the number of angular data that were compounded, the improvement obtained with an increase in the angular increments of 1°–3° (1 dB decrease) and 1°–5° (2 dB decrease) were not very large. Figure 11 presents SNR_e variations obtained from 3 (a), 5 (b), 7 (c), and 11 (d) beam-steered datasets for different maximum angles, respectively. The 0° dataset is included for all computations in this paper. Note that for only three beam-steered datasets, the SNR_e drops off with an increase in the maximum value of the steered angle. This is due to the noise artifacts introduced by larger insonification angles, where the SNR_e decreases about 7 dB for the largest steered angle of ±15° in Fig. 11(a). The maximum value of the SNR_e obtained with angular compounding for the axial strain image is around 30 dB, which is achieved for lower maximum steered angles of less than 10°. In a similar

manner in Fig. 9, smaller angular increments on the order of 1°–3°, also provide similar CNR_e results. For a maximum angle of 15°, 11 beam-steered datasets at 3° increments provide similar performance as 31 beam-steered datasets at 1° angular increments. In general, an optimal number of beam-steered datasets would be the most appropriate for a given maximum value of the beam-steered angle. However, it is difficult to determine a generic value of an optimum angular increment and maximum angle as it would also depend on the transducer center frequency, bandwidth, and array transducer construction parameters that would determine side-lobes and grating lobes. In general, from our results for the system and transducer utilized, the SNR_e and CNR_e are maximized for angular increments around 3° and maximum angles less than 10°.

Several investigators have also reported on the use of only three beam-steered datasets to estimate both axial and lateral displacement vectors and strain tensors.[21,30] The premise employed by these investigators is that the 0° dataset would provide axial strain information, while the beam-steered data acquired at the largest possible steered angle could be utilized for lateral strain computation by estimation of the lateral components along the beam-steered data. Larger beam-steered angles provide more lateral deformation information at the cost of introducing additional noise artifacts into both the strain tensor images. Larger steered angles improve lateral strain estimation, however, the impact of grating lobes and other noise artifacts have to be considered especially for linear array transducers. However, these larger beam-steered angles also significantly reduce both the SNR_e and CNR_e in the axial strain images as illustrated in Fig. 11(a) for the three datasets obtained at the 0° and ±15° angular increments.

The discussion in the above two paragraphs demonstrates the opposing and competing requirements if one attempts to maximize the SNR_e and CNR_e in both the axial and lateral strain tensors utilizing the same beam-steered datasets. Maximizing the SNR_e and CNR_e for axial strain imaging requires smaller angular increments and lower maximum steered angles as illustrated in this paper. On the other hand, accurate lateral strain imaging require larger beam-steered angles.[15,21]

Several tradeoffs therefore have to be considered, if one proposes to minimize the number of beam-steered angles for clinical applications. If the temporal resolution is important, for example, for imaging moving structures fewer angles should be utilized. On the other hand, if the spatial resolution and improvement in the SNR_e and CNR_e is the deciding parameter, more beam-steered datasets can be included in the computation to maximize the SNR_e and CNR_e obtained. Computational aspects with beam steering have also to be considered for clinical applications. In our implementation, beam-steered data acquisition was inefficient since it was performed using a script on a laptop to control the data acquisition. Processing of the beam-steered RF datasets was also performed using MATLAB. Computationally efficient implementations of both 1D and 2D processing exist that would enable us to obtain angular displacements in real-time. However, reductions in the frame-rate for strain imaging will definitely occur with the use of a larger number of steered angles for angular compounding. In addition, beam steering, data acquisition, and processing have to be implemented on the ultrasound system to further improve computational efficiency.

ACKNOWLEDGMENTS

This work was supported by Komen Grant No. BCTR0601153 and National Institutes of Health (NIH)-Cancer Institute (NCI) Grant Nos. 5R21CA140939-02, R01CA112192-S103, and R01CA112192-05.

[a]Electronic mail: hxu26@wisc.edu
[b]Author to whom correspondence should be addressed. Electronic mail: tvarghese@wisc.edu; Telephone: (608) 265-8797; Fax: (608) 262-2413.

[1]H. Xu, T. Varghese, and E. L. Madsen, "Analysis of shear strain imaging for classifying breast masses: Finite element and phantom results," Med. Phys. **38**, 6119–6127 (2011).
[2]H. Xu, M. Rao, T. Varghese, S. Baker, A. M. Sommer, T. J. Hall, E. S. Burnside, and G. A. Sisney, "Axial-shear strain imaging for differentiating benign and malignant breast masses," Ultrasound Med. Biol. **36**, 1813–1824 (2010).
[3]A. Thitaikumar, L. M. Mobbs, C. M. Kraemer-Chant, B. S. Garra, and J. Ophir, "Breast tumor classification using axial shear strain elastography: A feasibility study," Phys. Med. Biol. **53**, 4809–4823 (2008).
[4]E. E. Konofagou, T. Harrigan, and J. Ophir, "Shear strain estimation and lesion mobility assessment in elastography," Ultrasonics **38**, 400–404 (2000).
[5]T. Varghese, M. Bilgen, and J. Ophir, "Multiresolution imaging in elastography," IEEE Trans. Ultrason. Ferroelectr. Freq. Control **45**, 65–75 (1998).
[6]R. Righetti, J. Ophir, and P. Ktonas, "Axial resolution in elastography," Ultrasound Med. Biol. **28**, 101–113 (2002).
[7]S. Srinivasan, R. Righetti, and J. Ophir, "Trade-offs between the axial resolution and the signal-to-noise ratio in elastography," Ultrasound Med. Biol. **29**, 847–866 (2003).
[8]H. Chen, H. Shi, and T. Varghese, "Improvement of elastographic displacement estimation using a two-step cross-correlation method," Ultrasound Med. Biol. **33**, 48–56 (2007).
[9]Y. Zhu and T. Hall, "A modified block matching method for real-time freehand strain imaging," Ultrason. Imaging **24**, 161–176 (2002).
[10]R. Righetti, S. Srinivasan, and J. Ophir, "Lateral resolution in elastography," Ultrasound Med. Biol. **29**, 695–704 (2003).
[11]M. Rao and T. Varghese, "Spatial angular compounding for elastography without the incompressibility assumption," Ultrason. Imaging **27**, 256–270 (2005).
[12]M. Rao, Q. Chen, H. Shi, and T. Varghese, "Spatial-angular compounding for elastography using beam steering on linear array transducers," Med. Phys. **33**, 618–626 (2006).
[13]M. Rao, Q. Chen, H. Shi, T. Varghese, E. L. Madsen, J. A. Zagzebski, and T. Wilson, "Normal and shear strain estimation using beam steering on linear-array transducers," Ultrasound Med. Biol. **33**, 57–66 (2007).
[14]M. Rao, T. Varghese, and E. L. Madsen, "Shear strain imaging using shear deformations," Med. Phys. **35**, 412–423 (2008).
[15]U. Techavipoo, Q. Chen, T. Varghese, and J. A. Zagzebski, "Estimation of displacement vectors and strain tensors in elastography using angular insonifications," IEEE Trans. Med. Imaging **23**, 1479–1489 (2004).
[16]M. A. Lubinski, S. Y. Emelianov, K. R. Raghavan, A. E. Yagle, A. R. Skovoroda, and M. O'Donnell, "Lateral displacement estimation using tissue incompressibility," IEEE Trans. Ultrason. Ferroelectr. Freq. Control **43**, 247–256 (1996).
[17]I. Cespedes, Y. Huang, J. Ophir, and S. Spratt, "Methods for estimation of subsample time delays of digitized echo signals," Ultrason. Imaging **17**, 142–171 (1995).
[18]F. Viola and W. F. Walker, "A spline-based algorithm for continuous time-delay estimation using sampled data," IEEE Trans. Ultrason. Ferroelectr. Freq. Control **52**, 80–93 (2005).
[19]E. Konofagou and J. Ophir, "A new elastographic method for estimation and imaging of lateral displacements, lateral strains, corrected axial strains and Poisson's ratios in tissues," Ultrasound Med. Biol. **24**, 1183–1199 (1998).
[20]J. Luo and E. E. Konofagou, "Effects of various parameters on lateral displacement estimation in ultrasound elastography," Ultrasound Med. Biol. **35**, 1352–1366 (2009).

[21]H. H. Hansen, R. G. Lopata, T. Idzenga, and C. L. de Korte, "Full 2D displacement vector and strain tensor estimation for superficial tissue using beam-steered ultrasound imaging," Phys. Med. Biol. **55**, 3201–3218 (2010).
[22]S. Korukonda and M. M. Doyley, "Estimating axial and lateral strain using a synthetic aperture elastographic imaging system," Ultrasound Med. Biol. **37**, 1893–1908 (2011).
[23]R. G. Lopata, M. M. Nillesen, H. H. Hansen, I. H. Gerrits, J. M. Thijssen, and C. L. de Korte, "Performance evaluation of methods for two-dimensional displacement and strain estimation using ultrasound radio frequency data," Ultrasound Med. Biol. **35**, 796–812 (2009).
[24]F. Viola, R. L. Coe, K. Owen, D. A. Guenther, and W. F. Walker, "Multidimensional spline-based estimator (MUSE) for motion estimation: algorithm development and initial results," Ann. Biomed. Eng. **36**, 1942–1960 (2008).
[25]R. Z. Azar, O. Goksel, and S. E. Salcudean, "Sub-sample displacement estimation from digitized ultrasound RF signals using multi-dimensional polynomial fitting of the cross-correlation function," IEEE Trans. Ultrason. Ferroelectr. Freq. Control **57**, 2403–2420 (2010).
[26]Q. Chen, A. L. Gerig, U. Techavipoo, J. A. Zagzebski, and T. Varghese, "Correlation of RF signals during angular compounding," IEEE Trans. Ultrason. Ferroelectr. Freq. Control **52**, 961–970 (2005).
[27]U. Techavipoo, Q. Chen, T. Varghese, J. A. Zagzebski, and E. L. Madsen, "Noise reduction using spatial-angular compounding for elastography," IEEE Trans. Ultrason. Ferroelectr. Freq. Control **51**, 510–520 (2004).
[28]U. Techavipoo and T. Varghese, "Improvements in elastographic contrast-to-noise ratio using spatial-angular compounding," Ultrasound Med. Biol. **31**, 529–536 (2005).
[29]M. Rao and T. Varghese, "Correlation analysis for angular compounding in strain imaging," IEEE Trans. Ultrason. Ferroelectr. Freq. Control **54**, 1903–1907 (2007).
[30]R. Z. Azar, O. Goksel, and S. Salcudean, "Comparison between 2-D cross correlation with 2-D sub-sampling and 2-D tracking using beam steering," IEEE Trans. Ultrason. Ferroelectr. Freq. Control **58**, 1534–1537 (2011).
[31]G. M. Treece, A. H. Gee, and R. W. Prager, "Ultrasound compounding with automatic attenuation compensation using paired angle scans," Ultrasound Med. Biol. **33**, 630–642 (2007).
[32]R. Z. Azar, A. Baghani, S. E. Salcudean, and R. Rohling, "2-D high-frame-rate dynamic elastography using delay compensated and angularly compounded motion vectors: Preliminary results," IEEE Trans. Ultrason. Ferroelectr. Freq. Control **57**, 2421–2436 (2010).
[33]T. Varghese and J. Ophir, "The nonstationary strain filter in elastography: Part I. Frequency dependent attenuation," Ultrasound Med. Biol. **23**, 1343–1356 (1997).
[34]T. Varghese, "Quasi-static ultrasound elastography," Ultrasound Clin. **4**, 323–338 (2009).
[35]E. L. Madsen, M. A. Hobson, H. Shi, T. Varghese, and G. R. Frank, "Stability of heterogeneous elastography phantoms made from oil dispersions in aqueous gels," Ultrasound Med. Biol. **32**, 261–270 (2006).
[36]E. L. Madsen, M. A. Hobson, G. Frank, H. Shi, J. Jiang, T. J. Hall, T. Varghese, M. M. Doyley, and J. B. Weaver, "Anthropomorphic breast phantoms for testing elastography systems," Ultrasound Med. Biol. **32**, 857–874 (2006).
[37]T. Varghese and J. Ophir, "An analysis of elastographic contrast-to-noise ratio," Ultrasound Med. Biol. **24**, 915–924 (1998).
[38]I. Cespedes and J. Ophir, "Reduction of image noise in elastography," Ultrason. Imaging **15**, 89–102 (1993).
[39]T. Varghese and J. Ophir, "A theoretical framework for performance characterization of elastography: The strain filter," IEEE Trans. Ultrason. Ferroelectr. Freq. Control **44**, 164–172 (1997).